

ARTICLE

Open Access

# Perovskite quantum dot-induced monochromatization for broadband photodetection of wafer-scale molybdenum disulfide

Minji Kim<sup>1,2</sup>, Garam Bae<sup>1,3</sup>, Kyeong Nam Kim<sup>1</sup>, Hyeong-ku Jo<sup>1</sup>, Da Som Song<sup>1</sup>, Seulgi Ji<sup>1</sup>, Dohyun Jeon<sup>1</sup>, Semin Ko<sup>4</sup>, Seon Joo Lee<sup>1</sup>, Sungho Choi<sup>4</sup>, Soonmin Yim<sup>1</sup>, Wooseok Song<sup>1</sup>, Sung Myung<sup>1</sup>, Dae Ho Yoon<sup>2</sup>, Ki-Seok An<sup>1</sup> and Sun Sook Lee<sup>1</sup>

## Abstract

Two-dimensional transition metal dichalcogenide (2D TMD) crystals are versatile platforms for realizing emergent optoelectronic devices. However, the ability to produce large-area 2D TMDs with spatial homogeneity and to accomplish broadband photodetection by tuning the operating wavelengths in photodetectors are two paramount prerequisites for practical applications of 2D TMD-based photodetectors. Here, we demonstrated all-solution-processed broadband photodetectors based on the wafer-scale perovskite quantum dots (PQDs)/MoS<sub>2</sub> through light management *via* the monochromatization effect of the PQDs. The photodetectors exhibited broadband photodetection behavior that retained high photocurrents over a wide spectral range (254, 365, and 532 nm) by enhancing the photoresponse in the UV region through light management *via* the monochromatization effect of the PQDs. This intriguing strategy was proven with (i) electrical isolation realized by inserting an Al<sub>2</sub>O<sub>3</sub> insulator between the PQDs and MoS<sub>2</sub> and (ii) alteration of the PQD density. The rational nanohybrid-based photodetectors also exhibited superb air stability and exceptional bending durability.

## Introduction

Because of their restricted dimensionality, two-dimensional transition metal dichalcogenides (2D TMDs) have been used to enhance the capabilities of many nanophotonic applications, and have especially provided paradigm shifts in the realms of highly flexible, low power consumption, and high-performance optoelectronic devices<sup>1–4</sup>. Despite the many intriguing and

superb properties of 2D TMDs, two prerequisites for practical application in photodetectors remain elusive. The problems include (i) the lack of a reproducible technique for producing large-area 2D TMDs with spatial homogeneity for compatibility with conventional device manufacturing processes involving top-down lithographic fabrication and (ii) a lack of innovative strategies for the broadband photodetection and tunability of the operating wavelengths in photodetectors. Although meeting these prerequisites would enable the realization of broadband photodetector arrays with marginal variations in device-to-device performances, no such platform has yet been developed. To solve the first problem, a massive effort has been directed toward producing TMDs via direct chalcogenization of predeposited metal or metal oxide films, coevaporation of metal and chalcogen sources using

Correspondence: Wooseok Song ([wssong@kriict.re.kr](mailto:wssong@kriict.re.kr)) or Ki-Seok An ([ksan@kriict.re.kr](mailto:ksan@kriict.re.kr)) or Sun Sook Lee ([sunsukl@kriict.re.kr](mailto:sunsukl@kriict.re.kr))  
<sup>1</sup>Thin Film Materials Research Center, Korea Research Institute of Chemical Technology (KRICT), 141 Gajeong-ro, Yuseong-gu, Daejeon 34114, Republic of Korea  
<sup>2</sup>SKKU Advanced Institute of Nanotechnology (SAINT), Sungkyunkwan University, Suwon 16419, Republic of Korea  
Full list of author information is available at the end of the article  
These authors contributed equally: Minji Kim, Garam Bae

© The Author(s) 2022, corrected publication 2022

 **Open Access** This article is licensed under a Creative Commons Attribution 4.0 International License, which permits use, sharing, adaptation, distribution and reproduction in any medium or format, as long as you give appropriate credit to the original author(s) and the source, provide a link to the Creative Commons license, and indicate if changes were made. The images or other third party material in this article are included in the article's Creative Commons license, unless indicated otherwise in a credit line to the material. If material is not included in the article's Creative Commons license and your intended use is not permitted by statutory regulation or exceeds the permitted use, you will need to obtain permission directly from the copyright holder. To view a copy of this license, visit <http://creativecommons.org/licenses/by/4.0/>.

face-to-face metal precursors, and a metal-organic chemical vapor deposition (MOCVD) process<sup>5–10</sup>. We previously developed a large-area compatible, solution-based synthetic route for 2D MoS<sub>2</sub> layers, which has notable advantages, including relative simplicity, high cost-effectiveness, and potential for mass production<sup>11–13</sup>. To solve the second problem, various attempts have been made to employ complementary construction of TMD heterostructures *via* vertical stacking and coplanar stitching and TMD ternary semiconductors to manipulate the bandgap because the operating wavelengths of optoelectronic devices are largely dictated by the bandgaps of their photoactive materials<sup>14–18</sup>. Despite considerable efforts to tailor the electronic structure of TMD materials for actively tunable optoelectronic devices, no substantial progress has been made in this direction to achieve broadband photodetection. To address these issues, the primary goal of this study is to establish the unprecedented concept of a nanohybrid system composed of perovskite quantum dots (PQDs) and 2D MoS<sub>2</sub> for use in all-solution-processed, wafer-scale broadband photodetectors. A limitation of previous studies was that PQD/MoS<sub>2</sub> hybrid systems were focused on boosting the photoresponses of hybrid-based photodetectors *via* photo-induced interfacial charge transfer from PQDs with excellent light absorption coefficients to MoS<sub>2</sub><sup>19</sup>. We focused on the overlooked phenomenon of monochromatizing PQDs without photon-induced direct charge interaction between the PQDs and MoS<sub>2</sub>. To the best of our knowledge, this is the first demonstration of a broadband photodetector based on PQDs/MoS<sub>2</sub> that achieves light management *via* the monochromatization effect of PQDs. This strategy also enables large-scale production of 2-inch PQDs/MoS<sub>2</sub> broadband photodetectors with excellent uniformity and high flexibility for high performance, which are prerequisites to overcoming the limitations of Si-based broadband photodetectors<sup>20,21</sup>.

## Materials and methods

### Chemicals

Cesium carbonate (Cs<sub>2</sub>CO<sub>3</sub>, 99%), lead bromide (PbBr<sub>2</sub>, ≥98%), octanoic acid (OTAc, ≥99%), didodecyltrimethylammonium bromide (DDAB, 98%), oleylamine (OAM, 90%), 1-octadecene (ODE, 90%), oleic acid (OA, 90%), ethyl acetate (anhydrous, 99.8%), methyl acetate (anhydrous, 99.5%), and toluene (anhydrous, 99.8%) were purchased from Sigma-Aldrich (St. Louis, USA). Formamidinium acetate (FA(Ac), 99%) and ammonium tetrathiomolybdate ((NH<sub>4</sub>)<sub>2</sub>MoS<sub>4</sub>, 99.95%) were purchased from Acros Organics (New Jersey, USA). Ethyl acetate (99.5%, EP) was purchased from Samchun Chemical (Seoul, Korea). Hydroiodic acid (HI, 57%) was purchased from Alfa-Aesar (Ward Hill, USA). All chemicals were used without further purification.

### Synthesis of Cs<sub>0.85</sub>FA<sub>0.15</sub>PbBr<sub>3</sub> quantum dots

Cs<sub>0.85</sub>FA<sub>0.15</sub>PbBr<sub>3</sub> QDs were synthesized according to the literature with minor modification<sup>22</sup>. To prepare the Cs-FA precursor, 0.425 mol of Cs<sub>2</sub>CO<sub>3</sub> and 0.15 mol of FA(Ac) were loaded into a 10 mL vial and dissolved in 5 mL of OTAc by sonication. For the Pb precursor, 1 mmol of PbBr<sub>2</sub> and 2 mmol of TOAB were dissolved in 10 mL of toluene by sonication. After the PbBr<sub>2</sub> was completely dissolved, 9 mL of the PbBr<sub>2</sub> solution was loaded into a 25 mL beaker, and then 1 mL of the Cs-FA precursor was quickly added into the beaker at room temperature with vigorous stirring. After 5 min, 3 mL of DDAB solution (0.0432 M) was added to the reaction mixture and held for 2 min. For purification, ethyl acetate was added to the crude solution, and the precipitate was collected by centrifugation at 10,000 rpm for 10 min. The precipitate was dispersed in toluene, and additional centrifugation with ethyl acetate was conducted. Finally, the resulting QDs were redispersed in 4 mL of toluene.

### Synthesis of CsPbBr<sub>3</sub> quantum dots

To prepare Cs-oleate, Cs<sub>2</sub>CO<sub>3</sub> (0.542 g), and OA (1.66 mL) were mixed with ODE (20 mL) in a three-neck flask and degassed under vacuum at room temperature for 1.5 h. The solution was heated to 140 °C under vacuum for 1 h, and then the dissolved solution was stirred under N<sub>2</sub> for 7 min. To prepare OAM-HI, OAM (10 mL) and HI (4.8 mL) were mixed with diethyl ether (200 mL). The mixed solution was stirred for 1 h and then degassed under vacuum. OAM-HI was diluted with toluene. PbBr<sub>2</sub> (0.2760 g), OA (2 mL), and OAM (2 mL) were mixed with ODE (20 mL) in a three-neck flask and degassed under vacuum at 120 °C for 1 h to synthesize CsPbBr<sub>3</sub>. The dissolved solution was heated to 180 °C under N<sub>2</sub>, and then Cs-oleate (2.5 mL) was quickly injected into the flask. After 30 s, the solution was cooled in an ice-water bath. For the anion exchange reaction, OAM-HI (16 mL) was quickly injected into the CsPbBr<sub>3</sub> crude solution under N<sub>2</sub> flow at room temperature. The resulting solution was stirred under N<sub>2</sub> for 30 min in an ice-water bath. Finally, purification processes were implemented. The solution was centrifuged at 12,000 rpm for 15 min, after which the supernatant was discarded. The precipitate was dissolved in toluene (10 mL) and ethyl acetate (15 mL) with a 1:1.5 volume ratio. The solution was centrifuged again. Then, the supernatant was discarded, and the precipitate was dispersed in hexane (5 mL).

### Solution-based synthesis of large-area MoS<sub>2</sub> layers

A large-area compatible, solution-based synthetic route for 2D MoS<sub>2</sub> layers was carried out by using a simple coating of an (NH<sub>4</sub>)<sub>2</sub>MoS<sub>4</sub> single source precursor with subsequent two-step thermal decomposition techniques<sup>12</sup>. First, 1.25 wt% (NH<sub>4</sub>)<sub>2</sub>MoS<sub>4</sub> as a single source

precursor was stirred into ethylene glycol at room temperature for 60 min. Then, the as-prepared solution was spin-coated onto hydrophilic-treated SiO<sub>2</sub> (300 nm)/Si substrates, during which the rotational speed and rotation time were prudently configured to be 3000 rpm and 40 s, respectively. The coated samples were immediately annealed at 100 °C for 1 min to remove the solvent. The samples were annealed at 280 °C (first step) by introducing Ar (1000 sccm) at a pressure of 1 Torr for 30 min and subsequently annealed at 600 °C (second step) for 30 min to synthesize the MoS<sub>2</sub> layers. The synthesized MoS<sub>2</sub> layers were transferred onto polyimide (PI) and polyurethane (PU) films *via* surface energy-assisted wet transfer using a polystyrene support layer<sup>23,24</sup>.

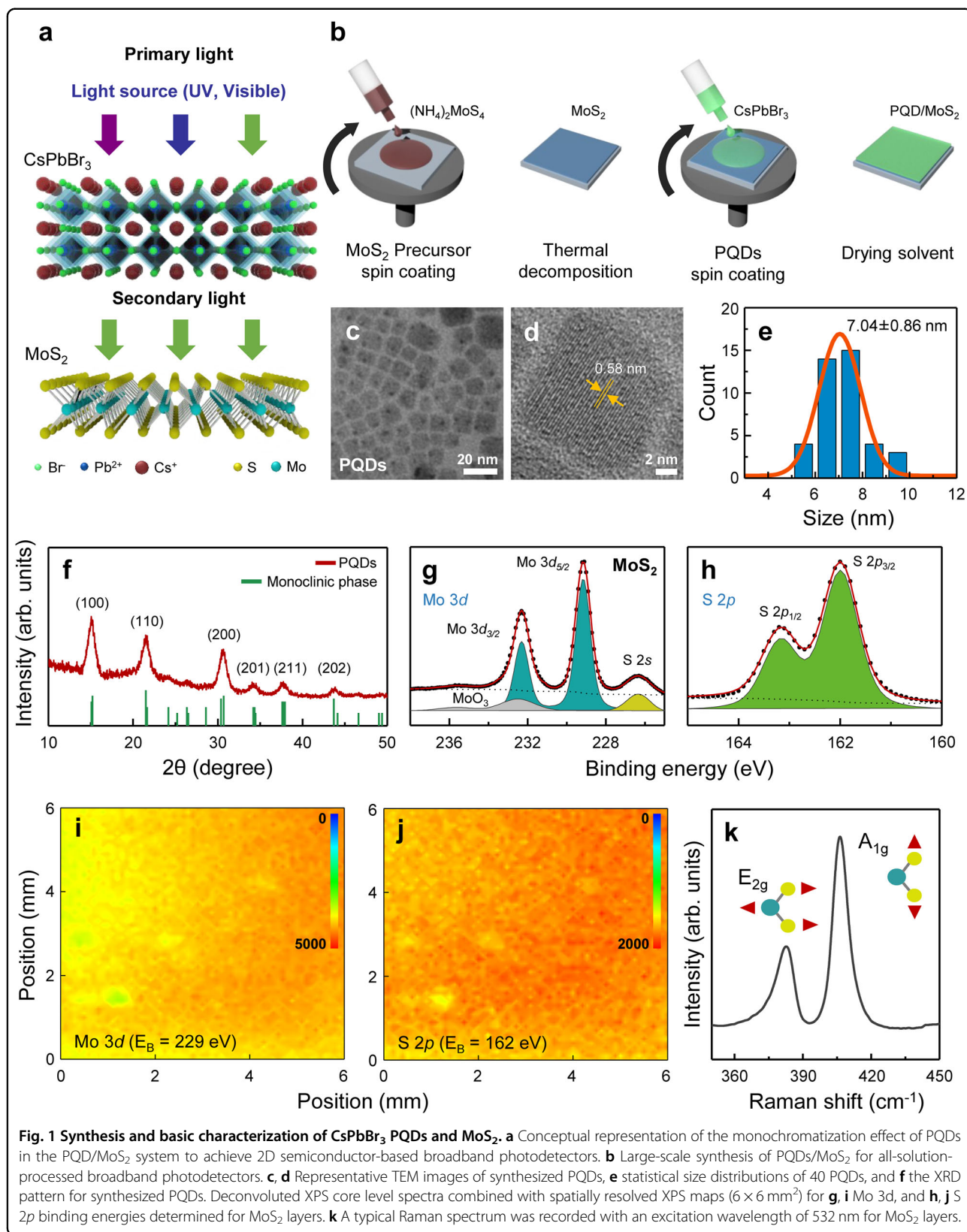
### Characterization

Structural characterization of the PQDs/MoS<sub>2</sub> was performed with transmission electron microscopy (TEM, Titan Cube G2 60–300, FEI company), atomic force microscopy (AFM, Multimode 8, Bruker), and Raman spectrometry (inVia system, Renishaw Inc.) coupled with an optical microscope (BX53MTRFS, Olympus). X-ray diffraction (XRD) patterns of the PQDs were obtained with a D/Max 2200 (Rigaku) diffractometer with monochromatic Cu K $\alpha$  radiation ( $\lambda = 1.54 \text{ \AA}$ ,  $h\nu = 8.0478 \text{ keV}$ ) in a Bragg–Brentano geometry. The X-ray tube voltage and current were adjusted to 40 kV and 40 mA, respectively. The scan range and scan rates were 10–50° and 2.5°/min, respectively. Raman spectroscopy was implemented with an excitation wavelength of 532 nm. The incident laser power irradiated on the samples was adjusted to 30 mW/cm<sup>2</sup>. Chemical identification of the samples was conducted with X-ray photoelectron spectroscopy (XPS, K-alpha, Thermo Scientific) equipped with a 180° double focusing hemispherical analyzer and a 128-element multichannel detection system. XPS analysis was performed with a normal emission geometry using conventional microfocused monochromatic Al K $\alpha$  radiation ( $h\nu = 1486.6 \text{ eV}$ ) with a spot size of 500 × 500  $\mu\text{m}^2$ . The pass energy was adjusted to 50.0 eV with a step size of 0.1 eV.

### Results and discussion

Herein we propose an unprecedented rational hybrid system for accomplishing 2D semiconductor-based broadband photodetectors. We focused on “light management” *via* the monochromatization effect of the PQDs instead of the typical route involving optimization of the inherent properties of materials *via* “material management”. Figure 1a gives a pictorial representation of the strategy used for managing the light induced by monochromatization of the PQDs through the rational coupling of the 2D MoS<sub>2</sub> and PQDs. Specifically, initial irradiation with primary light involved multiple wavelengths that

caused photoluminescent (PL) emission of monochromatic visible light from the PQDs, leading to irradiation of secondary light with a rectified wavelength on the visible-light-sensitive MoS<sub>2</sub>. This enabled the realization of broadband photodetectors based on PQDs/MoS<sub>2</sub>. A detailed methodology for the synthesis of PQDs/MoS<sub>2</sub> is described in the experimental section. We selected a previously established idea to develop a large-area compatible, solution-based synthetic route for 2D MoS<sub>2</sub> layers using a simple coating of an (NH<sub>4</sub>)<sub>2</sub>MoS<sub>4</sub> single source precursor with a subsequent two-step thermal decomposition technique<sup>11,12</sup>. Large-scale syntheses of PQDs/MoS<sub>2</sub> were carried out with a sequential coating of a perovskite Cs<sub>0.85</sub>FA<sub>0.15</sub>PbBr<sub>3</sub> QD solution on the synthesized MoS<sub>2</sub> layers, as illustrated in Fig. 1b. The merits of this synthetic route are its feasibility and reliability for large-scale production of PQDs/MoS<sub>2</sub> for all-solution-processed broadband photodetectors. To exploit the monochromatization effect of the PQDs in the PQD/MoS<sub>2</sub> system, comprehensive microscopic and spectroscopic evaluations of the inherent properties of individual low-dimensional materials were performed. Figure 1c, d exhibits representative TEM images of the synthesized PQDs, which indicate that well-defined, rectangular-shaped PQDs were acquired, and the interplanar spacing of the PQD crystal was estimated to be 0.58 nm; this represented the (100) plane in the monoclinic structure of the PQDs<sup>22</sup>. Figure 1e shows the statistical size distribution of the 40 PQDs and corroborates the formation of PQDs with a narrow size distribution (mean size: 7.04 ± 0.86 nm). We anticipate that the formation of uniformly sized PQDs will offer key advantages in terms of reliable performance for photodetectors based on PQDs/MoS<sub>2</sub> because the size-dependent quantum confinement effects of low-dimensional nanomaterials exhibit strong correlations with their electronic band structures. XRD measurements were performed on the synthesized PQDs to establish crystallinity; these studies revealed the monoclinic phase structure, in good agreement with the TEM results (Fig. 1f)<sup>22</sup>. Further insights into the chemical bonding of the PQDs were acquired by using XPS (Supporting Information Fig. S1). Based on the XPS spectra, the atomic ratios of Cs, Pb, and Br were estimated to be 1:1.06:3.40, implying that formation of nearly stoichiometric PQDs resulted. Four key elements, including Mo, S, Si, and O, were identified in the survey spectrum for MoS<sub>2</sub> synthesized on SiO<sub>2</sub>/Si using a large-area compatible solution-based synthetic route (Supporting Information Fig. S2). The deconvoluted Mo 3d and S 2p core level spectra acquired from MoS<sub>2</sub> synthesized on SiO<sub>2</sub>/Si are displayed in Fig. 1g, h, respectively. Each spectrum was fitted using a Gaussian-Lorentzian function and sharp background subtraction. The Mo 3d core level spectrum for synthesized MoS<sub>2</sub> revealed doublet peaks composed of



Mo<sup>4+</sup> bonded in the trigonal prismatic lattice of MoS<sub>2</sub> ( $E_B = 229.1$  and  $232.3$  eV) and Mo<sup>6+</sup> states for MoO<sub>3</sub> ( $E_B = 232.5$  and  $235.7$  eV), along with the S 2s state ( $E_B = 226.3$  eV). In the S 2p core level region, there was a doublet related to the S 2p<sub>3/2</sub> ( $E_B = 162.0$  eV) and S 2p<sub>1/2</sub> ( $E_B = 163.1$  eV) states in MoS<sub>2</sub>. It is worth noting that the marginal formation of an oxide with higher binding energy than MoS<sub>2</sub> was discernible, indicating that the synthetic conditions presented for the synthesis of MoS<sub>2</sub> are well established. The atomic ratio of S and Mo was estimated to be 2.2. Figure 1i, j presents spatially resolved XPS maps ( $6 \times 6$  mm<sup>2</sup>) extracted from the Mo 3d ( $E_B = 229$  eV) and S 2p ( $E_B = 162$  eV) core level spectra of MoS<sub>2</sub> on SiO<sub>2</sub>. These results implied excellent spatial homogeneity for the atomic distributions of Mo and S over a large area ( $6 \times 6$  mm<sup>2</sup>), which is important for the realization of device arrays with analogous responses for industrial applications in nanophotonic devices. Figure 1k presents a typical Raman spectrum recorded with an excitation wavelength of 532 nm for MoS<sub>2</sub> layers synthesized using a solution-based large-area compatible approach, and the spectrum indicated showed two peaks for the in-plane E<sub>2g</sub> and out-of-plane A<sub>1g</sub> phonon modes<sup>25</sup>. The difference in wavenumbers for these two Raman active phonon modes was  $23.6$  cm<sup>-1</sup>, which suggests the preparation of a few-layer morphology for MoS<sub>2</sub><sup>26</sup>.

To validate the large-scale spatial homogeneity, we fabricated PQD/MoS<sub>2</sub>-based photodetector arrays on a 2-inch SiO<sub>2</sub>/Si wafer, as displayed in Fig. 2a, b, which are representative photographic images obtained with visible light (photograph) and UV light (fluorescence image), respectively. The color contrast of the photograph was marginal. The homogeneous PL emission from the PQDs was discernible over a large area except for near the electrodes, which show excellent homogeneity in the film thickness. To verify the long-range spatial homogeneity, we further analyzed PL spectra for PQDs/MoS<sub>2</sub> recorded at 30 arbitrary locations. The PL excitation peaks were located at 514 nm, and their spectral line shapes were nearly identical, which indicated excellent homogeneity over a large area (Supporting Information Fig. S3). In addition, structural and elemental studies of the PQDs/MoS<sub>2</sub> were performed to enable light management via the monochromatization effect of the PQDs. First, cross-sectional TEM observations were used to explore the structural features of PQDs/MoS<sub>2</sub>, as displayed in Fig. 2c, d. There were several important features noticeable in these TEM observations: (1) MoS<sub>2</sub> was completely covered with the PQD layer and (2) the number of MoS<sub>2</sub> layers and thicknesses of the PQDs were 13 and 37 nm, respectively. MoS<sub>2</sub> monolayers have been regarded as ideal candidates for many nanophotonic applications owing to the inherent direct bandgap induced by their low

dimensionality<sup>2</sup>. From an application viewpoint, however, a multilayer system offers critical merits such as stronger photon absorption, a longer photoexcited carrier lifetime, air stability, and narrow fluctuations of the band structure caused by altering the number of layers<sup>27–29</sup>. These features are important for forming photodetector arrays with reliable performance and consistent responses from all devices. An energy-dispersive X-ray spectroscopy (EDS) map generated with a scanning TEM (STEM) image of the PQDs/MoS<sub>2</sub> corroborated the atomic distributions of Cs and Pb extracted from the PQD layer, Mo from MoS<sub>2</sub>, and Si from SiO<sub>2</sub>, which confirmed that MoS<sub>2</sub> was completely covered with the PQD layer, as displayed in Fig. 2e–j. Figure 2k exhibits a typical AFM topographical image of the as-synthesized MoS<sub>2</sub> on SiO<sub>2</sub> (300 nm)/Si(001), from which the root-mean-square (RMS) roughness was assessed to be 0.69 nm. After hybridization, morphological alterations of PQDs/MoS<sub>2</sub> were readily discriminated by considering an RMS roughness of 5.41 nm, which resembled the surface morphology of the as-received PQDs with an RMS roughness of 4.16 nm, as represented in Fig. 2l–n. Next, we determined the normal Stokes PL emission of the synthesized PQDs to shed light on the rectified secondary light of the PQDs in the nano-hybrid system. Figure 2o–r reveals PL spectra and fluorescence photographs generated with an excitation wavelength of 365 nm and acquired for the PQD solution, as-coated PQD films, PQDs/MoS<sub>2</sub>, and MoS<sub>2</sub>. The PL excitation peaks of all samples were located at 516 nm, in accordance with values reported in prior literature<sup>22</sup>. However, discernible variations in the intensities of PL peaks originating from the green emissive PQDs were generated by altering the PQD content used during sample preparation, in good agreement with the fluorescence photographs. Intriguingly, the intensities of the PL peaks for PQDs/MoS<sub>2</sub> decayed markedly compared with those of the as-coated PQD films formed under identical coating conditions. This observation suggested that the PL emitted from the PQDs was strongly absorbed in the surfaces of the MoS<sub>2</sub> layers. These results from the AFM and PL studies afforded clear evidence for complete encapsulation of the PQDs on MoS<sub>2</sub> and strong absorption of PL emitted from the PQDs, which enabled light management *via* the monochromatization effects of the PQDs. Figure 2s presents UV–vis–NIR absorption spectra of the PQDs, MoS<sub>2</sub>, and PQDs/MoS<sub>2</sub>, and two distinctive results were readily discernible: (1) hybridization of the MoS<sub>2</sub> and PQDs enabled simultaneous absorption of UV and visible light photons and (2) the PQDs exhibited nearly 100% transmittance of 532-nm photons. Based on these results, we can anticipate the monochromatization effects of the PQD/MoS<sub>2</sub> system, as depicted in Fig. 2t. Irradiation with 254 and 365 nm light led to secondary light originating from PL emission of

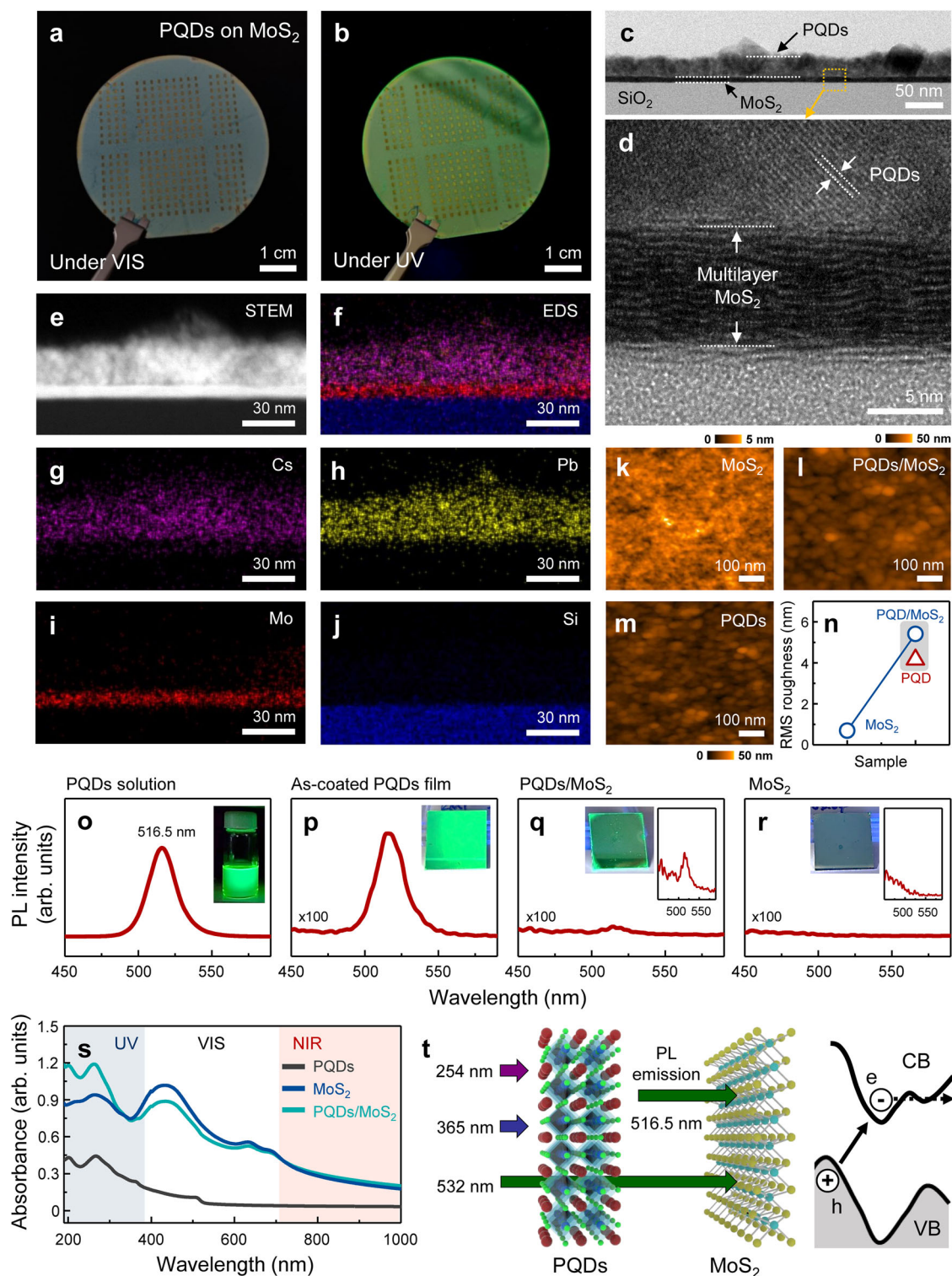


**Fig. 2 Structural and optical properties of hybridized PQDs/MoS<sub>2</sub>.** Photographs of PQDs/MoS<sub>2</sub>-based photodetector arrays on 2 in. SiO<sub>2</sub>/Si wafer under **a** visible light and **b** UV light. **c, d** Representative cross-sectional TEM images of PQDs/MoS<sub>2</sub>. **e** STEM image and EDS elemental maps of **f** all elements, **g** Cs, **h** Pb, **i** Mo, and **j** Si for the PQDs/MoS<sub>2</sub> on SiO<sub>2</sub> (300 nm)/Si(001). Typical AFM topographical images of **k** as-synthesized MoS<sub>2</sub>, **l** PQDs/MoS<sub>2</sub>, and **m** PQDs on SiO<sub>2</sub> (300 nm)/Si(001). **n** Plot of the RMS roughnesses of MoS<sub>2</sub>, as-received PQDs, and PQDs/MoS<sub>2</sub>. PL spectra and (inset) fluorescence photographs with an excitation wavelength of 365 nm were acquired from **o** the PQD solution, **p** as-coated PQDs, **q** PQDs/MoS<sub>2</sub>, and **r** MoS<sub>2</sub>. **s** UV-vis-NIR absorption spectra obtained for the PQDs, MoS<sub>2</sub>, and PQDs/MoS<sub>2</sub>. **t** Pictorial representation of the monochromatization effects in the PQD/MoS<sub>2</sub> system.

monochromatic visible light ( $\lambda = 516.5$  nm) from the PQDs, which subsequently irradiated the visible-light sensitive 2D MoS<sub>2</sub>. Additionally, a transmittance of nearly 100% was ascertained for primary photons with a wavelength of 532 nm passing through the PQD layer. Consequently, rectified visible-light photons were irradiated on the MoS<sub>2</sub>, which yielded a high photocurrent caused by photoinduced carrier excitation of MoS<sub>2</sub> to realize a photodetector with large spectral coverage and demonstrate performance optimization of the photoconductive device. Additionally, the XPS peaks in the survey spectrum showing the MoS<sub>2</sub> bonding states and two distinctive Raman active phonon modes for MoS<sub>2</sub> were completely absent after hybridization, which reinforced our findings from the foregoing TEM and AFM results (Supporting Information Fig. S4)<sup>30,31</sup>.

To prepare broadband photodetectors, we fabricated PQD/MoS<sub>2</sub>-based photodetectors by forming electrical contacts (70-nm-thick Au/3-nm-thick Cr) via thermal evaporation with a shadow mask, and the channel lengths and widths were 100 and 600  $\mu\text{m}$ , respectively, as displayed in Fig. 3a. The incident photon wavelengths were adjusted to 254 (0.35 mW/cm<sup>2</sup>), 365 (0.26 mW/cm<sup>2</sup>), and 532 nm (20 mW/cm<sup>2</sup>). The representative time-dependent photocurrents of the MoS<sub>2</sub>- and PQDs/MoS<sub>2</sub>-based photodetectors were examined for periodic photon illumination with wavelengths of 254, 365, and 532 nm, as seen in Fig. 3b–g. The photocurrents of pristine MoS<sub>2</sub>-based photodetectors reached 0.12 nA at 20 V (254 nm), 0.21 nA at 20 V (365 nm), and 13 nA at 20 V (532 nm), which indicated the wavelength-dependent photoconductive behavior of pristine MoS<sub>2</sub>. Astonishingly, the photocurrents for the PQD/MoS<sub>2</sub>-based photodetectors were unequivocally amplified to 8.88 nA at 20 V (254 nm) and 9.94 nA at 20 V (365 nm), reflecting broadband photodetection caused by light management via the monochromatization effect of the PQDs. The photon-stimulated and reliable switching behavior of the photocurrents from the PQD/MoS<sub>2</sub>-based photodetectors were shown for repeated illumination with 532 nm light (Supporting Information Fig. S5). A large discrepancy in the rise/decay times for UV (254 and 365 nm) and visible light (532 nm) illumination resulted from the setup for wavelength-dependent measurements, which was composed of single UV lamps and a visible-light laser integrated with a mechanical chopper to modulate the frequency of the light source. The photoresponsivity and detectivity values extracted determined for the PQD/MoS<sub>2</sub>-based photodetectors were 55.81 (254 nm), 47.23 (365 nm), and 1.05 mA/W (532 nm) at 20 V and 5.20 (254 nm), 3.12 (365 nm), and 1.18 cm Hz<sup>1/2</sup> W<sup>-1</sup> (532 nm), respectively. The minimum response times for the photodetectors were 7.7 (254 nm), 7.4 (365 nm), and 0.085 s (532 nm). For comparison, we summarized the

photoresponse characteristics of MoS<sub>2</sub>-based photodetectors from previously reported literature (Supporting Information Table S1). We traced compelling clues to validate our suggestions for light management via the monochromatization effects of the PQDs. First, we considered whether broadband photodetection by PQD/MoS<sub>2</sub> due to the monochromatization effect could be influenced by altering the PQD density because the photoresponse in the UV regime was optimized by complete encapsulation of the PQDs on MoS<sub>2</sub>. To tune the PQD density, the concentration of PQDs was manipulated by dilution with hexane to give 100% PQD, 10% PQD, and 1% PQD solutions. Appreciable decreases in the intensities of the PL excitation peaks seen for concentration-tailored PQDs accompanied decreases in the concentrations of PQDs, as shown by the fluorescence photographs in the insets in Fig. 3h–j. A better structural understanding of the concentration-tailored PQDs on MoS<sub>2</sub> was obtained by using TEM, as displayed in Fig. 3k. It is noteworthy that reliable control of the PQD density was attained by regulating the concentration of the PQD solution. Conversely, the inherent structural features of the MoS<sub>2</sub> bottom layers were invariant after coupling with the density-modulated PQDs (Supporting Information Fig. S6). Additional Raman spectroscopy results coupled with AFM observations showed that two distinctive Raman active phonon modes correlated with MoS<sub>2</sub> emerged with decreasing the PQD density, and noticeable variations in the PQD densities were observed after altering the concentration of the PQD solution, which replicated the TEM observations (Supporting Information Fig. S7). Fluorescence photographs recorded with an excitation wavelength of 365 nm and time-dependent photocurrents induced by illumination at 254 and 365 nm for the density-modulated PQDs on MoS<sub>2</sub>-based photodetectors are shown in Fig. 3l–n. Notably, we ascertained that the PQD density largely dictated both the fluorescence intensities and photocurrents of the PQD/MoS<sub>2</sub>-based photodetectors. The strong correlation between PQD density resulting from the solution concentration and the photocurrents of the photodetectors is presented in Fig. 3o. In the PQD/MoS<sub>2</sub> hybrid system, complete encapsulation of the PQDs on MoS<sub>2</sub> yielded rectified secondary light that stimulated photoinduced carrier excitation of the 2D MoS<sub>2</sub>. With a decrease in the PQD density, direct irradiation of the primary UV light source without the monochromatization of the PQDs resulted in photocurrent deterioration.

In previous studies, PQD/MoS<sub>2</sub> hybrid systems were restricted to boosting the photoresponses of hybrid-based photodetectors. The enhanced photoresponse can be interpreted as photoinduced interfacial charge transfer from PQDs to MoS<sub>2</sub> with an excellent light absorption coefficient, which influenced energy band bending and

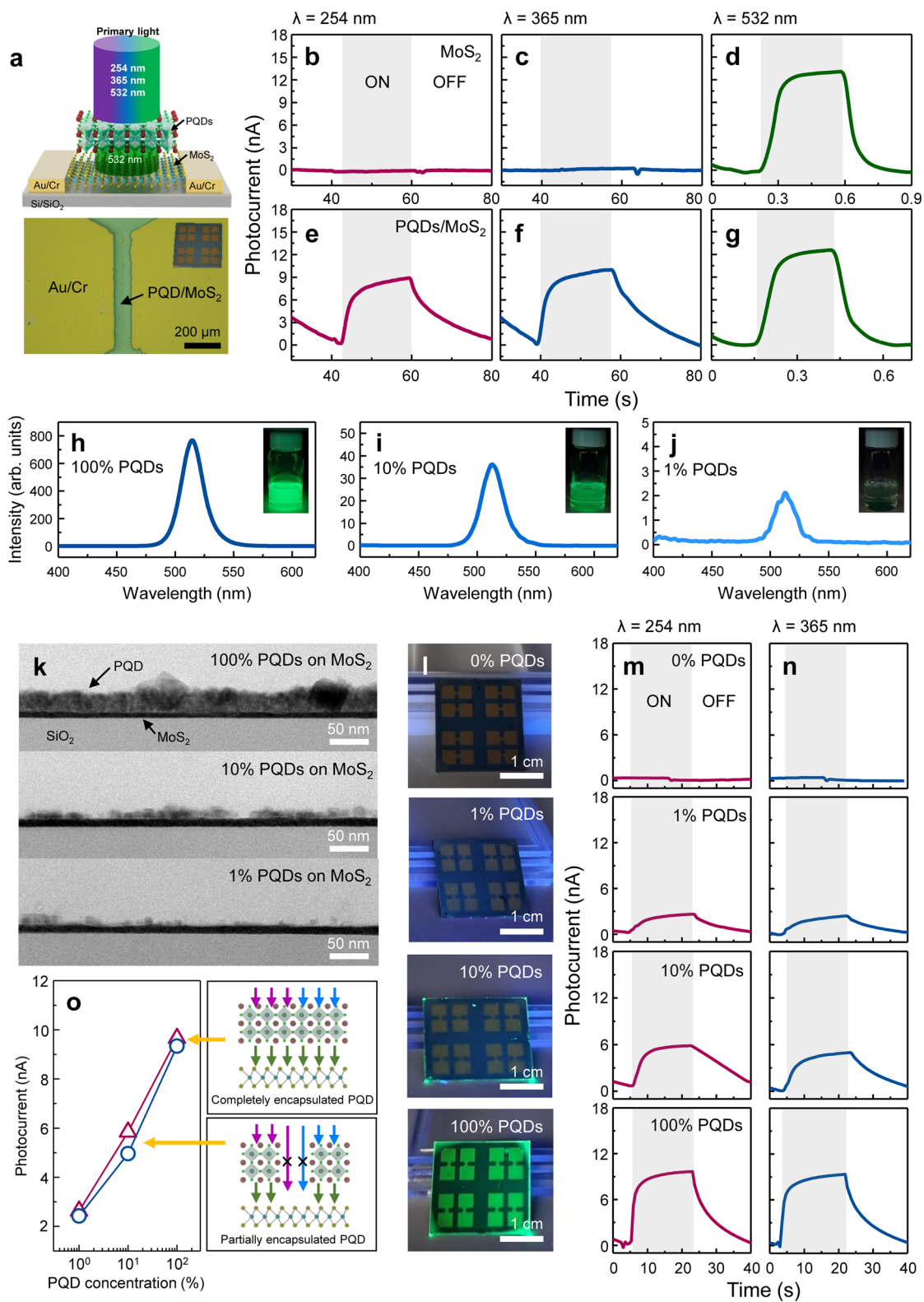


**Fig. 3** (See legend on next page.)

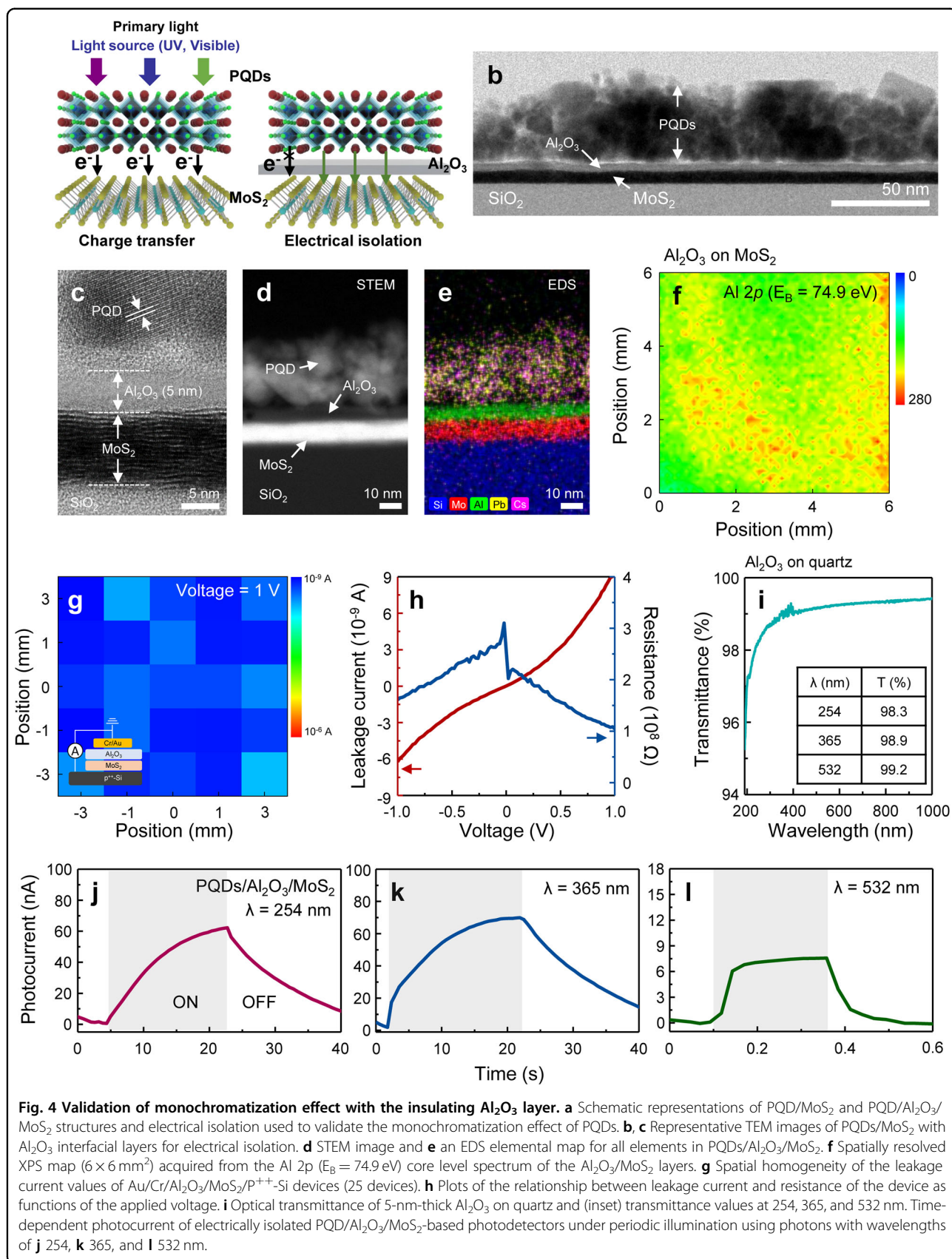
(see figure on previous page)

**Fig. 3 Monochromatization effect on PQDs/MoS<sub>2</sub>.** **a** Schematic illustration and a representative optical microscope image of a PQD/MoS<sub>2</sub>-based photodetector. Time-dependent photocurrents of the **b–d** MoS<sub>2</sub>- and **e–g** PQDs/MoS<sub>2</sub>-based photodetectors under periodic photon illumination with wavelengths of 254, 365, and 532 nm. PL spectra and (inset) fluorescence photographs were obtained with an excitation wavelength of 365 nm for **h** 100% PQD, **i** 10% PQD, and **j** 1% PQD solutions. **k** TEM images of concentration-tailored PQDs on MoS<sub>2</sub>. **l** Fluorescence photographs recorded with an excitation wavelength of 365 nm and time-dependent photocurrents induced by photon illumination with wavelengths of **m** 254 nm and **n** 365 nm for coverage-modulated PQDs on MoS<sub>2</sub>-based photodetectors. **o** Photocurrents of completely encapsulated PQDs/MoS<sub>2</sub> and partially encapsulated PQDs/MoS<sub>2</sub> as a function of PQD concentration.

formation of the depletion region<sup>19,32,33</sup>. We focused on the overlooked approach involving monochromatization of the PQDs in the PQD/MoS<sub>2</sub> hybrid system for high-performance photodetection with broad spectral coverage. Second, we placed Al<sub>2</sub>O<sub>3</sub> layers located between the PQDs and MoS<sub>2</sub> for electrical isolation to confirm the monochromatization effect, which can be ruled out by direct charge transfer from the PQDs to MoS<sub>2</sub>, as depicted in Fig. 4a. The presented strategy was developed with comprehensive examinations involving TEM, EDS, XPS, and electrical measurements. Figure 4b, c shows representative TEM images of PQDs/MoS<sub>2</sub> with Al<sub>2</sub>O<sub>3</sub> interfacial layers for electrical isolation, and three distinctive features can readily be discerned: (1) insertion of Al<sub>2</sub>O<sub>3</sub> continuous layers was readily discernable, (2) the thickness of the Al<sub>2</sub>O<sub>3</sub> layer was approximately 5 nm, and (3) the inherent layered structure of MoS<sub>2</sub> was well preserved after deposition of the Al<sub>2</sub>O<sub>3</sub>. Chemical identification of the PQD/Al<sub>2</sub>O<sub>3</sub>/MoS<sub>2</sub> hybrid layers was conducted with EDS elemental mapping combined with STEM observations, which demonstrated that well-defined PQD/Al<sub>2</sub>O<sub>3</sub>/MoS<sub>2</sub> hybrid layers were discernible, as displayed in Fig. 4d, e. Figure 4f shows a spatially resolved XPS map (6 × 6 mm<sup>2</sup>) acquired from the Al 2p (E<sub>B</sub> = 74.9 eV) core level spectrum of the Al<sub>2</sub>O<sub>3</sub>/MoS<sub>2</sub> layers, which indicated the formation of a homogeneous Al<sub>2</sub>O<sub>3</sub> layer on MoS<sub>2</sub> over a large area. Direct evidence for electrical isolation inhibiting photoinduced carrier transfer from the PQDs to MoS<sub>2</sub> was acquired by examining the spatial homogeneity of the leakage currents for Au/Cr/Al<sub>2</sub>O<sub>3</sub>/MoS<sub>2</sub>/P<sup>++</sup>-Si devices (25 devices), as revealed in Fig. 4g. It can be seen that 100% active devices with large areas (6 × 6 mm<sup>2</sup>) were studied, and their average leakage current was ~10<sup>-9</sup> A, which was attributed to complete electrical isolation caused by the Al<sub>2</sub>O<sub>3</sub> interfacial layer. Figure 4h presents plots of the relationships between leakage current and resistance of the devices as functions of the applied voltage, which clearly reflect electrical insulation by the Al<sub>2</sub>O<sub>3</sub>. Figure 4i shows the optical transmittance of 5-nm-thick Al<sub>2</sub>O<sub>3</sub> on quartz, indicating that the optical transmittances at 254, 365, and 532 nm were 98.3, 98.9, and 99.2%, respectively. From the foregoing results, we used Al<sub>2</sub>O<sub>3</sub> interfacial layers with high optical transmittance values for electrical isolation to validate the monochromatization effect of PQDs. The representative

time-dependent photocurrents of the electrically isolated PQDs/Al<sub>2</sub>O<sub>3</sub>/MoS<sub>2</sub>-based photodetectors were evaluated for periodic illumination with photons with wavelengths of 254, 365, and 532 nm, as shown in Fig. 4j–l. As anticipated, the photocurrents of the PQD/Al<sub>2</sub>O<sub>3</sub>/MoS<sub>2</sub>-based photodetectors realized with irradiation at 254 and 365 nm were indisputably boosted, which indicated the monochromatization effect of the PQDs without direct charge transfer. The discernible discrepancies in the photocurrents resulting from UV (254 and 365 nm) illumination of the PQD/Al<sub>2</sub>O<sub>3</sub>/MoS<sub>2</sub>- and PQDs/MoS<sub>2</sub>-based photodetectors resulted from differences in the thicknesses of the PQD layers on Al<sub>2</sub>O<sub>3</sub> (39 nm) and MoS<sub>2</sub> (27 nm), which were related to the surface hydrophobicity.

In both PQDs and 2D semiconductor systems, the structural instability associated with their low-dimensional natures leads to unavoidable oxidation, which causes device performance to deteriorate and arguably distinguishes them from bulk materials. Thus, air stability is indispensable for practical optoelectronic applications. We validated the sustainability of the photoelectrical performance, including the photocurrent, response time (a maximum photocurrent of 90%), and recovery time (a minimum photocurrent of 10%), for PQD/MoS<sub>2</sub> broadband photodetectors over 180 days in the air, as indicated in Fig. 5a–c; the data showed superb air stability with only slight deteriorations of the response times (Supporting Information Fig. S8). In addition, we validated the capability of PQDs/MoS<sub>2</sub> for flexible optoelectronic applications. The synthesized PQDs/MoS<sub>2</sub> was transferred to a PI film *via* surface energy-assisted wet transfer using a polystyrene support layer<sup>23,24</sup>. Mechanical bending durability tests of the PQD/MoS<sub>2</sub>-based flexible photodetectors were carried out by monitoring the time-dependent photocurrent resulting from periodic photon illumination as a function of the bending radius (R = 4, 2.5, 2, and 1 mm) (Supporting Information Fig. S9). Figure 5d displays photographs of the periodic bending-releasing machine utilized to examine the bending durability of the device. The bending radius-independent stability of the photocurrent was discernible for all wavelengths, as presented in Fig. 5e. Surprisingly, the photocurrent of the device was nearly identical after repeated tests (10<sup>5</sup> cycles) under harsh bending conditions (bending radius = 1 mm), indicating exceptional bending durability



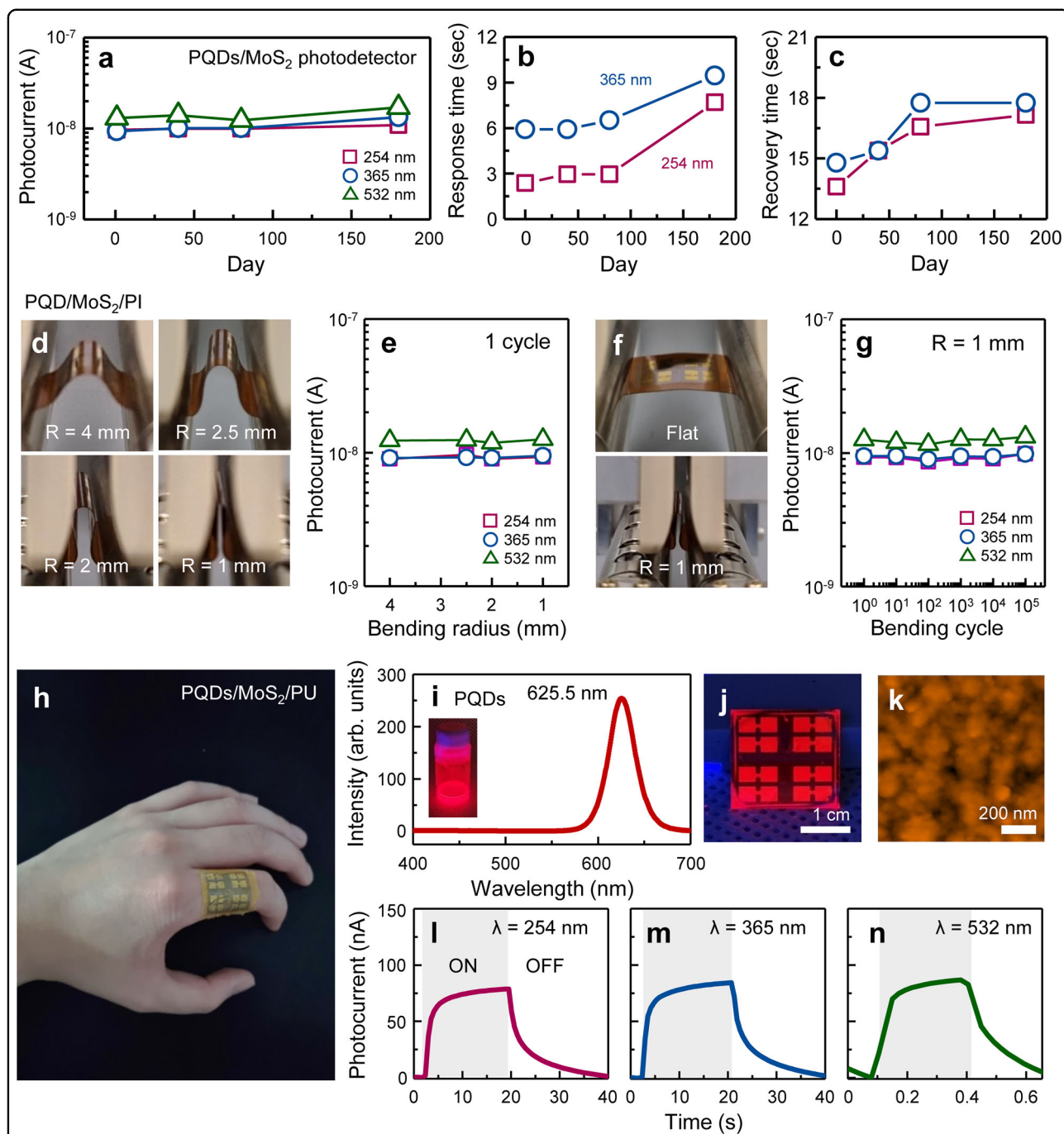


**Fig. 5 Long-term stability, bending durability, and universal applicability of PQDs/MoS<sub>2</sub>.** Sustainability of **a** photocurrent, **b** response time, and **c** recovery time (10% minimum photocurrent) for PQD/MoS<sub>2</sub> broadband photodetectors over 180 days in the air. **d, f** Photographs of a periodic bending-releasing machine used to examine bending durability. Plots of the photocurrents of the PQD/MoS<sub>2</sub> broadband photodetectors under periodic illumination with wavelengths of 254, 365, and 532 nm as functions of **e** the bending radius (1 cycle) and **g** bending cycles (R = 1 mm). **h** Proof-of-concept demonstration for flexible and broadband photodetectors fabricated on a PU and intimately integrated with the human hand. **i** PL spectrum and (inset) a fluorescence photograph with an excitation wavelength of 365 nm acquired from the red-emissive PQD solution. **j** A fluorescence photograph and **(k)** AFM image of a red PQD/MoS<sub>2</sub>-based photodetector. Time-dependent photocurrents of the red PQD/MoS<sub>2</sub>-based photodetector under periodic photon illumination with wavelengths of **l** 254, **m** 365, and **n** 532 nm.

for all wavelengths, as exhibited in Fig. 5f, g and Supporting Information Fig. S9. The excellent flexibility made it possible to intimately integrate the device with the human hand, which signaled the promising potential for application with flexible and wearable optoelectronic devices, as demonstrated in Fig. 5h. To enable universal applicability of the monochromatization effect of PQDs to realize broadband photodetectors, we intend to extend the PQD/MoS<sub>2</sub> system by adopting red-emissive PQDs (CsPbBr<sub>2</sub>). Optical and structural characterizations of red-emissive PQDs were carried out with PL spectroscopy, fluorescence spectroscopy, and AFM observations, as exhibited in Fig. 5i–k. The chemical bonding states of the red PQDs were determined using XPS (Supporting Information Fig. S10). The PL excitation peak of the PQD solution was located at 625.5 nm, indicating the presence of red-emissive PQDs. We ascertained the formation of homogeneous red PQDs on MoS<sub>2</sub> over a large area (RMS roughness = 5.55 nm). It should be highlighted that the monochromatization effect of red PQDs was distinctly shown by increases in the photocurrents caused by irradiation at 254 and 365 nm, as shown in Fig. 5l–n, which affords an ideal platform for application in versatile nanophotonic devices based on 2D semiconductors.

## Conclusions

In conclusion, we presented a facile methodology for preparing broadband photodetectors based on large-scale PQDs/MoS<sub>2</sub> through light management *via* the monochromatization effect of the PQDs. To facilitate the monochromatization effect, the PQD/MoS<sub>2</sub> system was rationally designed, and explicit structural and chemical explorations of the individual low-dimensional materials were implemented. The resulting PQD/MoS<sub>2</sub>-based photodetectors revealed broadband photodetection behavior that retained high photocurrents over a wide spectral range. We traced compelling clues to confirm that our observations were strongly correlated to monochromatization by altering the PQDs density with electrical isolation caused by inserting an Al<sub>2</sub>O<sub>3</sub> insulator. In addition, the PQD/MoS<sub>2</sub> broadband photodetectors exhibited superb air stability and exceptional bending durability. We envisage that the approaches presented herein will afford an innovative strategy for broadband photodetection and tunability of the operating wavelengths in photodetectors as well as large-scale production of hybrid materials, thereby resolving two prerequisites that will have ramifications for emergent optoelectronic devices.

## Acknowledgements

This research was supported by the Nano-Material Technology Development Program through the National Research Foundation (NRF) of Korea, funded by the Ministry of Science and ICT (2021M3D1A2046733) and the Materials Innovation Project (2020M3H4A3081790) funded by NRF of Korea.

## Author details

<sup>1</sup>Thin Film Materials Research Center, Korea Research Institute of Chemical Technology (KRICT), 141 Gajeong-ro, Yuseong-gu, Daejeon 34114, Republic of Korea. <sup>2</sup>SKKU Advanced Institute of Nanotechnology (SAINT), Sungkyunkwan University, Suwon 16419, Republic of Korea. <sup>3</sup>Cambridge Graphene Centre, University of Cambridge, 9 JJ Thomson Avenue, Cambridge CB3 0FA, United Kingdom. <sup>4</sup>Energy Materials Research Center, Korea Research Institute of Chemical Technology (KRICT), 141 Gajeong-ro, Yuseong-gu, Daejeon 34114, Republic of Korea

## Author contributions

W.S., K.-S.A., and S.S.L. conceived the projects and designed the research. M.K. and G.B. performed the experiments and analyzed the results. K.N.K., H.-k.J., D.S.S., S.J., D.J., and S.K. provided help with the experiments. S.J.L., S.C., S.Y., S.M., and D.H.Y. wrote the manuscript and discussed it. All authors contributed to the writing of the paper.

## Conflict of interest

The authors declare no competing interests.

## Publisher's note

Springer Nature remains neutral with regard to jurisdictional claims in published maps and institutional affiliations.

**Supplementary information** The online version contains supplementary material available at <https://doi.org/10.1038/s41427-022-00435-y>.

Received: 27 April 2022 Revised: 7 September 2022 Accepted: 15 September 2022.

Published online: 18 November 2022

## References

- Wang, Q. H., Kalantar-Zadeh, K., Kis, A., Coleman, J. N. & Strano, M. S. Electronics and optoelectronics of two-dimensional transition metal dichalcogenides. *Nat. Nanotechnol.* **7**, 699–712 (2012).
- Lopez-Sanchez, O., Lembke, D., Kayci, M., Radenovic, A. & Kis, A. Ultrasensitive photodetectors based on monolayer MoS<sub>2</sub>. *Nat. Nanotechnol.* **8**, 497–501 (2013).
- Mak, K. F. & Shan, J. Photonics and optoelectronics of 2D semiconductor transition metal dichalcogenides. *Nat. Photonics* **10**, 216–226 (2016).
- Huo, N. & Konstantatos, G. Recent progress and future prospects of 2D-based photodetectors. *Adv. Mater.* **30**, 1801164 (2018).
- Zhan, Y., Liu, Z., Najmaei, S., Ajayan, P. M. & Lou, J. Large-area vapor-phase growth and characterization of MoS<sub>2</sub> atomic layers on a SiO<sub>2</sub> substrate. *Small* **8**, 966–971 (2012).
- Song, J. G. et al. Layer-controlled, wafer-scale, and conformal synthesis of tungsten disulfide nanosheets using atomic layer deposition. *ACS Nano* **7**, 11333–11340 (2013).
- Lin, W. S. et al. Selection role of metal oxides into transition metal dichalcogenide monolayers by a direct selenization process. *ACS Appl. Mater. Interfaces* **10**, 9645–9652 (2018).
- Yang, P. et al. Batch production of 6-inch uniform monolayer molybdenum disulfide catalyzed by sodium in glass. *Nat. Commun.* **9**, 979 (2018).
- Kang, K. et al. High-mobility three-atom-thick semiconducting films with wafer-scale homogeneity. *Nature* **520**, 656–660 (2015).
- Zhao, Y. et al. Low-temperature synthesis of 2D MoS<sub>2</sub> on a plastic substrate for a flexible gas sensor. *Nanoscale* **10**, 9338–9345 (2018).
- Lim, Y. R. et al. Wafer-scale, homogeneous MoS<sub>2</sub> layers on plastic substrates for flexible visible-light photodetectors. *Adv. Mater.* **28**, 5025–5030 (2016).
- Lim, Y. R. et al. Roll-to-roll production of layer-controlled molybdenum disulfide: a platform for 2D semiconductor-based industrial applications. *Adv. Mater.* **30**, 1705270 (2018).
- Lim, Y. R. et al. Atomic-level customization of 4 in. transition metal dichalcogenide multilayer alloys for industrial applications. *Adv. Mater.* **31**, 1901405 (2019).
- Novoselov, K. S., Mishchenko, A., Carvalho, A. & Castro Neto, A. H. 2D materials and van der Waals heterostructures. *Science* **353**, 461 (2016).

15. Kang, K. et al. Layer-by-layer assembly of two-dimensional materials into wafer-scale heterostructures. *Nature* **550**, 229–233 (2017).
16. Gong, Y. et al. Vertical and in-plane heterostructures from  $WS_2/MoS_2$  monolayers. *Nat. Mater.* **13**, 1135–1142 (2014).
17. Calman, E. V. et al. Indirect excitons in van der Waals heterostructures at room temperature. *Nat. Commun.* **9**, 1895 (2018).
18. Yao, J., Zheng, Z. & Yang, G. Promoting the performance of layered-material photodetectors by alloy engineering. *ACS Appl. Mater. Interfaces* **8**, 12915–12924 (2016).
19. Wu, H. et al. All-inorganic perovskite quantum dot-Monolayer  $MoS_2$  mixed-dimensional van der Waals heterostructure for ultrasensitive photodetector. *Adv. Sci.* **5**, 1801219 (2018).
20. Alam, M. J. et al. Enhancing responsivity and detectivity in broadband UV-VIS photodetector by ex-situ UV-ozone annealing technique. *Superlattic. Microstruct.* **137**, 106333 (2022).
21. Rong, P. et al. A solution-processed octahedral nano-blocks structure  $CaIn_2S_4$  film for UV/vis photodetection. *Nanotechnology* **33**, 245709 (2022).
22. Song, J. et al. Room-temperature triple-ligand surface engineering synergistically boosts ink stability, recombination dynamics, and charge injection toward EQE-11.6% perovskite QLEDs. *Adv. Mater.* **30**, 1800764 (2018).
23. Gurarslan, A. et al. Surface-energy-assisted perfect transfer of centimeter-scale monolayer and few-layer  $MoS_2$  films onto arbitrary substrates. *ACS Nano* **8**, 11522–11528 (2014).
24. Lim, Y. R. et al. Resist- and etching-free patterning mediated by predefined photosensitive polyimide for two-dimensional semiconductor-based photodetectors. *Adv. Mater. Interfaces* **8**, 2001817 (2021).
25. Molina-Sánchez, A. & Wirtz, L. Phonons in single-layer and few-layer  $MoS_2$  and  $WS_2$ . *Phys. Rev. B* **84**, 155413 (2011).
26. Wang, X., Feng, H., Wu, Y. & Jiao, L. Controlled synthesis of highly crystalline  $MoS_2$  flakes by chemical vapor deposition. *J. Am. Chem. Soc.* **135**, 5304–5307 (2013).
27. Choi, W. et al. High-detectivity multilayer  $MoS_2$  phototransistors with spectral response from ultraviolet to infrared. *Adv. Mater.* **24**, 5832–5836 (2012).
28. Lee, Y. et al. Synthesis of wafer-scale uniform molybdenum disulfide films with control over the layer number using a gas phase sulfur precursor. *Nanoscale* **6**, 2821–2826 (2014).
29. Zhao, Z. Y. & Liu, Q. L. Study of the layer-dependent properties of  $MoS_2$  nanosheets with different crystal structures by DFT calculations. *Catal. Sci. Technol.* **8**, 1867–1879 (2018).
30. Wang, H., Zhang, C. & Rana, F. Surface recombination limited lifetimes of photoexcited carriers in few-layer transition metal dichalcogenide  $MoS_2$ . *Nano Lett.* **15**, 8204–8210 (2015).
31. Femi-Oyetoro, J. et al. Structural stability of bilayer  $MoS_2$  in ambient air. *Adv. Mater. Interfaces* **8**, 2101188 (2021).
32. Xiufeng, S. et al. Boosting two-dimensional  $MoS_2/CsPbBr_3$  photodetectors via enhanced light absorbance and interfacial carrier separation. *ACS Appl. Mater. Interfaces* **10**, 2801–2809 (2018).
33. Joydip, G. et al. Solid-state synthesis of stable and color tunable cesium lead halide perovskite nanocrystals and the mechanism of high-performance photodetection in a monolayer  $MoS_2/CsPbBr_3$  vertical heterojunction. *J. Mater. Chem. C* **8**, 8917–8934 (2020).